water

MDPI

*Article*

# Enhanced Photo–Fenton Removal Efficiency with Core-Shell Magnetic Resin Catalyst for Textile Dyeing Wastewater Treatment

**Jie Zhong [1,2], Bin Yang [1,2,*], Yong Feng [1,2], Yang Chen [3], Li-Gao Wang [3], Wen-Dan You [1,2] and Guang-Guo Ying [1,2,*]**

[1] Guangdong Provincial Key Laboratory of Chemical Pollution and Environmental Safety & MOE Key Laboratory of Theoretical Chemistry of Environment, SCNU Environmental Research Institute, South China Normal University, Guangzhou 510006, China; Jie.zhong@m.scnu.edu.cn (J.Z.); yong.feng@m.scnu.edu.cn (Y.F.); wendan.you@m.scnu.edu.cn (W.-D.Y.)

[2] School of Environment, South China Normal University, University Town, Guangzhou 510006, China

[3] Yulin Xintao Environmental Protection Technology Co., Ltd., Agile Environmental Protection Group, Yulin 537000, China; chenyang53@agile.com.cn (Y.C.); Wangligao@agile.com.cn (L.-G.W.)

* Correspondence: bin.yang@m.scnu.edu.cn (B.Y.); guangguo.ying@m.scnu.edu.cn (G.-G.Y.); Tel.: +86 020-39310536 (B.Y.); +86-020-39310796 (G.-G.Y.)

**Abstract:** Heterogeneous photo–Fenton reactions have been regarded as important technologies for the treatment of textile dyeing wastewaters. In this work, an efficient core-shell magnetic anion exchange resin (MAER) was prepared through in situ polymerization and used to remove reactive brilliant red (X-3B) in a UV–Fenton system. The MAER exhibited satisfactory removal efficiency for X-3B because of its highly effective catalytic activity. More than 99% of the X-3B (50 mg/L) was removed within 20 min in the UV–Fenton reaction. This is because the uniformly dispersed core-shell magnetic microsphere resin could suppress the aggregation of $Fe_3O_4$ nanoparticles and, thus, enhance the exposure of Fe reaction sites for catalytic reaction with $H_2O_2$. The good adsorption capacity of MAER also played an important role in promoting contact between X-3B and reactive radicals during the reaction. Mechanism research showed that hydroxyl radical (•OH) was the main reactive radicals for the removal of X-3B in the MAER UV–Fenton system. The MAER can be easily separated by a magnet after catalytic reactions. Moreover, the matrix effects of different substrates ($Cl^-$, $NO_3^-$, $SO_4^{2-}$, and humic acid) were investigated. The results showed that $SO_4^{2-}$ could be beneficial to improve the removal of X-3B but that the others decrease the removal. The MAER UV–Fenton also removed significant amounts of total organic carbon (TOC) for the X-3B solution and an actual textile dyeing industrial wastewater. The heterogeneous oxidation system established in this work may suggest prospects for practical applications in the treatment of textile dyeing wastewater.

**Keywords:** magnetic anion exchange resin (MAER); UV–Fenton; reactive brilliant red; textile dyeing wastewater

**Citation:** Zhong, J.; Yang, B.; Feng, Y.; Chen, Y.; Wang, L.-G.; You, W.-D.; Ying, G.-G. Enhanced Photo–Fenton Removal Efficiency with Core-Shell Magnetic Resin Catalyst for Textile Dyeing Wastewater Treatment. *Water* **2021**, *13*, 968. https://doi.org/10.3390/w13070968

Academic Editor: Naresh Singhal

Received: 23 February 2021
Accepted: 29 March 2021
Published: 31 March 2021



## 1. Introduction

As a representative of industrial organic wastewater, textile dyeing wastewater contains large numbers of refractory contaminants with high chroma and special smells, which are difficult to degrade using conventional chemical and activated sludge methods [1–3]. Advanced oxidation processes (AOPs) based on reactive oxidizing radicals are widely used in the treatment of organic wastewater due to the high degradation efficiencies of organic pollutants and their environmentally friendly nature [4,5]. The performance of AOPs for the degradation of refractory organic pollutants has been

evaluated by Fenton and Fenton-like processes [6], ozonation [7], photocatalysis [8], photo–Fenton [9], and electrochemical oxidation [10].

Fenton technology has been widely studied in organic wastewater treatment. In a Fenton process, hydrogen peroxide ($H_2O_2$) is catalyzed by $Fe^{2+}$ to generate various reactive oxidizing species in situ (e.g., hydroxyl radical ($^{\bullet}OH$) and superoxide anion radical ($^{\bullet}O_2^-$)). The reactive radicals with a high redox potential can easily degrade various refractory organic pollutants [11]. However, the valid pH range of the Fenton process is extremely narrow (pH = 2.5–3.5) and the organic pollutants cannot be fully mineralized. Many degradation products form complexes with $Fe^{3+}$, which inhibits the formation of $^{\bullet}OH$ and decreases the efficiency of the Fenton reaction [12–14]. By using photo–Fenton technologies, better removal efficiency can be obtained. UV irradiation and $Fe^{2+}$ have a synergistic effect on the catalytic decomposition of $H_2O_2$. The production rate of $^{\bullet}OH$ is much greater than the simple addition of $Fe^{2+}$ or UV photolysis alone. Moreover, the intermediate products generated in this process are photoactive matters [15], which could continue to be degraded under UV irradiation.

Homogeneous Fenton reactions also have other issues, such as the requirement for acid conditions and the formation of iron-containing sludge [16]. These limitations could be overcome by using heterogeneous solid catalyst-embedded inorganic magnetic materials. In recent years, magnetite ($Fe_3O_4$) has attracted extensive attention as a heterogeneous Fenton/photo–Fenton catalyst to degrade organic pollutants due to its low cost, easy separation, nontoxicity, and good stability. It has been reported that different types of $Fe_3O_4$-based catalysts, such as $Fe_3O_4$/reduced graphene oxide ($Fe_3O_4$/RGO) nanosheets [17], inverse-spinel ferroferric oxide nanoparticles decorated multiwalled carbon nanotubes ($Fe_3O_4$/MWCNTs) [18], and $Fe_3O_4$@GO@MIL-100(Fe) core-shells [19], are used in Fenton systems to improve the oxidation-activating ability and to accelerate target pollutant degradation. In such catalytic processes, Fe(Ⅲ) can be reversibly transformed to Fe(Ⅱ) in the octahedron of $Fe_3O_4$. However, magnetic $Fe_3O_4$ nanoparticles suffer from aggregation and stack in water, leading to decease of their specific surface area and catalytic activity. Therefore, $Fe_3O_4$-based catalysts combined with high adsorption capacity materials are a research focus that could enhance the generation of reactive radicals and the degradation of target pollutants.

Herein, an efficient catalyst using core-shell magnetic anion exchange resin (MAER) is synthesized by in situ polymerization. The core-shell structure of resin-coated magnetite could effectively alleviate the occurrence of agglomeration, thereby improving its catalytic performance. As a typical organic azo dye, reactive brilliant red (X-3B) dye was used as the target pollutant in this work (Table S1, Supplementary Material). The magnetic resin catalyst showed enhanced photo–Fenton removal efficiency for the X-3B. The objectives of this work were (1) to evaluate the catalytic reactivity of MAER, (2) to investigate the reactive species and removal mechanism of X-3B, and (3) to explore the practical application of MEAR in the treatment of actual textile dyeing wastewater.

## 2. Materials and Methods

### *2.1. Chemicals and Materials*

Polyvinyl alcohol (PVA) and polyvinyl pyrrolidone (PVP) were purchased from Sigma-Aldrich. Divinylbenzene, 4-chlorostyrene, dibenzoyl peroxide, 3-(trimethoxysilyl) propyl methacrylate (γ-MPS), tetraethyl orthosilicate (TEOS), *tert*-butanol, chloroform, trimethylamine solution, and heptane were purchased from Aladdin. Reactive brilliant red (X-3B) was purchased from Nanjing Dulai Biotechnology Co., Ltd. All other chemicals used in this study were analytical grade and purchased from Guangzhou Chemical Co. Ltd. Ultrapure water (≥18 MΩ cm) was used to prepare the experimental solutions. The actual textile dyeing wastewater was collected from a textile dyeing industrial factory in Guangxi Province (Figure S1) filtered through 0.45-μm

polyethersulfone (PES) membranes and then stored at 4 °C until use. The properties of textile dyeing wastewater are shown in Table S2.

### *2.2. Preparation of $Fe_3O_4$ Nanoparticles*

The $Fe_3O_4$ nanoparticles were prepared by a chemical co-precipitation method: 12.4 g of $FeCl_3 \cdot 6H_2O$ and 6.2 g of $FeCl_2 \cdot 4H_2O$ were dissolved in 200 mL of deionized water and stirred at 60 °C under a nitrogen atmosphere. $NH_4OH$ was then added dropwise until the pH value was adjusted to 10.0. Crystallization occurred and was maintained for 1 h. The magnetic particles were collected by centrifugation, washed with deionized water until neutral, and vacuum dried at 60 °C for 24 h.

### *2.3. Preparation of MAER*

The magnetic anion exchange resin (MAER) was prepared by a modified polymerization [20]. First, γ-MPS-modified $Fe_3O_4$ was prepared: 1.0 g of $Fe_3O_4$, 5.0 mL of $NH_4OH$, and 1.0 mL of TEOS were dispersed by ultrasonic treatment in 100 mL of ethanol, stirring at room temperature for 1 h; 2.0 mL γ-MPS was added and heated to 40 °C for 2 h to continue the reaction under a nitrogen atmosphere. The γ-MPS-modified $Fe_3O_4$ nanoparticles were washed with ethanol several times and dried. Second, the MAER was prepared through suspension polymerization: 5.0 mL of 4-chlorostyrene, 1.0 mL of divinylbenzene, 2.0 mL of heptanes, and 0.1 g of dibenzoyl peroxide were mixed, and then, 1.0 g of γ-MPS-modified $Fe_3O_4$ nanoparticles were ultrasonically dispersed into the above solution to obtain organic phase A. Fifty milliliters of deionized water, 0.4 g of PVA/0.4 g of PVP, and 2.0 g of NaCl were mixed and heated until dissolved to form aqueous phase B. Organic phase A and aqueous phase B were transferred to the reactor, heated to 80 °C for 3 h with stirring while the reactor filled with nitrogen atmosphere, and then heated to 90 °C for 3 h for further reaction to obtain a magnetic resin. After that, 10.0 mL of trimethylamine was added for aminolysis at 70 °C for 1 h. The resultant brown microspheres were obtained, washed with deionized water and ethanol several times, and vacuum dried at 60 °C for 24 h. A schematic illustration of the preparation of MAER is shown in Figure 1.

Similarly, without adding magnetic nanoparticles, anion exchange resin (AER) was synthesized by the above method.

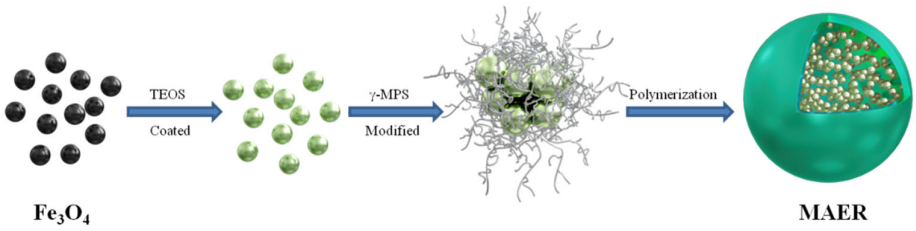


**Figure 1.** Schematic illustration of the preparation of magnetic anion exchange resin (MAER).

### *2.4. Removal Experiments*

Unless otherwise specified, all batch experiments were conducted in 50 mL centrifuge tubes at room temperature. An X-3B stock solution with a concentration of 200 mg/L was prepared in advance. For adsorption experiments, 20 mL of the diluted X-3B (50 mg/L) was transferred to the tube and 5.0 mg of material was added, stirring in a rotating shaker with a speed of 180 rpm. At the predetermined adsorption time, 2 mL of aliquots was extracted, filtered through 0.22 μm PES membranes (the recovery was about 99.4%), and used for measurement of the residual concentration. For removal experiments, a 300 W UV lamp was used as the light source with no filtering and the light signal was recorded using an AvaSpec-ULS4096CL-EVO (Avantes, Apeldoorn,

Netherlands) spectrophotometer equipped with an integrated sphere in the range of 200–800 nm [21], as shown in Figure S2. The light intensity was measured as 46.4 W/m$^2$. Then, 5.0 mg of material and a certain amount of $H_2O_2$ were added into the 20 mL reaction solutions of X-3B (50 mg/L) with magnetic stirring. Two milliliters of the aliquots were extracted at the predetermined time, filtered through 0.22 μm PES membranes, and quenched immediately with methanol (50 μL). To investigate the potential matrix effects on the UV–Fenton process, different types of coexisting constituents were added, including $Cl^-$, $NO_3^-$, $SO_4^{2-}$, and humic acid (HA). To evaluate the potential contribution of reactive radicals, tert-butanol and chloroform were employed as a quenching agent for $^{\bullet}OH$ and $^{\bullet}O_2^-$, respectively. For the actual textile dyeing wastewater, 2 mL of aliquots was extracted at predetermined time intervals, filtered using 0.22 μm PES membranes, and used for the measurement of total organic carbon (TOC). Except for investigating the effect of pH values, the pH of the reaction solution was not adjusted. All the batch experiments were repeated at least in duplicate.

### *2.5. Material Characterizations and Chemical Analysis*

The prepared materials were characterized as follows. Powder X-ray diffraction (XRD, D8-ADVANCE, Bruker, Shanghai, China) was used to characterize the crystalline structures. Fourier transform infrared spectroscopy (FT-IR, Nicolet 6700, ThermoFisher, Guangzhou, China) was used to study the functional groups on the material surfaces. X-ray photoelectron spectroscopy (XPS, ESCALab250, ThermoFisher, Guangzhou, China) was used to research the surface chemical compositions. The magnetic hysteresis loop was investigated using a vibrating sample magnetometer (VSM, MPMS3, Quantum, San Diego, USA). Thermo gravimetric analysis (TGA, STA409PC, NETZSCH, Selb, Germany) was used to measure the content of iron under air in the temperature range of 30–800 °C. The microstructures and the distribution of $Fe_3O_4$ into polymer were observed using a scanning electron microscope (SEM, Ultra-55, ZEISS, Oberkochen, Germany). A surface area analyzer (Micromeritics ASAP-2020, Shanghai, China) was used to measure the Brunauer–Emmett–Teller (BET)-specific surface area and pore size distribution under $N_2$ adsorption/desorption.

The concentration of X-3B was measured by 756-type optic spectrophotometric method at its maximum adsorption wave of 539 nm. The TOC was measured by a Shimadzu TOC-L analyzer. Electron spin resonance (ESR, JES FA-200, JEOL, Kyoto, Japan) was performed to detect the existence of reactive radicals using 5,5-dimethyl-1-pyrroline N-oxide (DMPO) as the spin trapping reagent.

## 3. Results and Discussion

### *3.1. Characterization of the Prepared Materials*

The crystalline structures of $Fe_3O_4$, AER, and MAER were characterized by XRD, as shown in Figure 2a. Obvious sharp peaks of $Fe_3O_4$ sample at $2\theta$ = 18.26° (111), 30.08° (220), 35.42° (311), 37.05° (222), 43.05° (400), 53.39° (422), 56.94° (511), and 62.51° (440) were assigned to the standard face center cubic phase of $Fe_3O_4$ (JCPDS no. 16-0629) [22]. These diffraction peaks were also observed in the MAER sample, demonstrating that $Fe_3O_4$ nanoparticles existed within the MAER. Meanwhile, a broad peak ranging from 18–23° in the MAER appeared, which can be also tracked in the AER sample. This result means that the resin was formed in an amorphous state. The FT-IR spectra of $Fe_3O_4$, AER, and MAER are shown in Figure 2b. The bending vibration of the Fe–O bond (about 600 cm$^{-1}$) can be observed in the $Fe_3O_4$ sample [23]. The characteristic peaks of AER and MAER were quite similar. A staggered adsorption peak was observed at 900–700 cm$^{-1}$ and a distinct peak at 1500 cm$^{-1}$. However, the MAER sample had a slight red-shift near the low frequency region at 1200–1300 cm$^{-1}$. This may be due to the combination of certain functional groups on the resin surface with Fe atom [24]. The XPS analysis was further performed to understand the compositions of Fe(II) and Fe(III) in the MAER catalyst, as shown in Figure

S3. Through the Fe 2p spectra result, the content of Fe(III) in MAER was calculated as 81.9% and that for Fe(II) was 18.1% [25]. The magnetic properties of $Fe_3O_4$ and MAER were evaluated by the hysteresis loops curve recorded at room temperature (Figure 2c). All these samples possessed typical paramagnetic behavior [26]. Although the saturation magnetization (Ms) of MAER (17.6 emu/g) was lower than that of $Fe_3O_4$ (69.6 emu/g), it was sufficient for separation from the aqueous solution by an external magnet (Figure 2c inset). The thermal stabilities of AER and MAER were measured to confirm the content of iron by TGA (Figure 2d). Slight weight loss (below 5 wt%) was observed under 200 °C, which was mainly ascribed to the evaporation of surface-adsorbed water. The two resins lost weight rapidly when the temperature was in the range of 200–450 °C, and the rate slowed down when the temperature was higher than 450 °C, mainly due to the thermal decomposition of the non-crosslinked and crosslinked areas of resin [27]. At about 600 °C, the two resins no longer lost weight. The content of $Fe_3O_4$ in the MAER was estimated to be around 14.8% by comparing the residual mass percentages of these two resins.

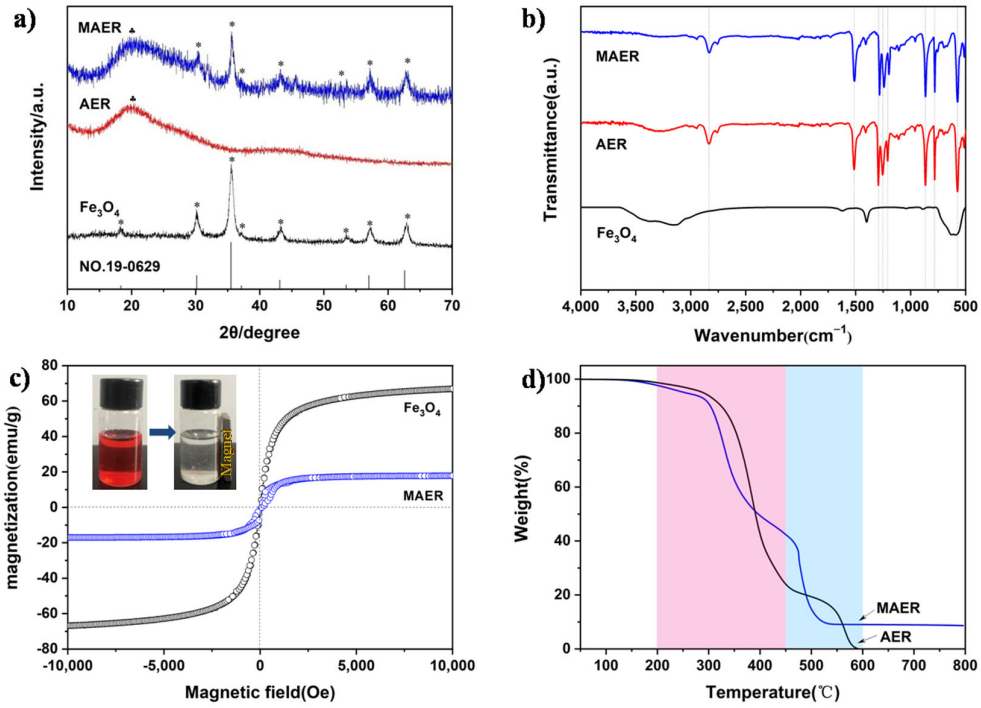


**Figure 2.** **a**) XRD patterns, **b**) FT-IR spectra, **c**) the magnetic hysteresis loops (the inset shows the separation process), and **d**) thermo gravimetric analysis (TGA) curves of the prepared materials.

The surface morphology and microstructure of MAER were investigated. As can be seen in Figure 3a, the MAER displayed spherical morphology with diameters in the range of 40 μm to 50 μm. Some pores and holes can be observed distributing on the MAER microspheres according to the high-magnification image (Figure 3d). This is because the magnetic nanoparticles and polymer precursors combine through small pieces during the reaction, then extend outward, and assemble into new microspheres. It can effectively alleviate the occurrence of agglomeration and introduce some active functional groups by coating the $Fe_3O_4$ outer layer with resinpolymer, compared with the SEM result of $Fe_3O_4$ (Figure S4). The BET surface area of MAER was estimated to be 18.7 $m^2/g$, and the pore size was mainly distributed in the range of 2–5 nm (Figure S5 and Table S3). By using EDS element line-scanning (Figure 3b), a Fe signal was detected within the microsphere (Figure 3c), suggesting that the magnetic microspheres were coated with resins to form core-shell structures [20].

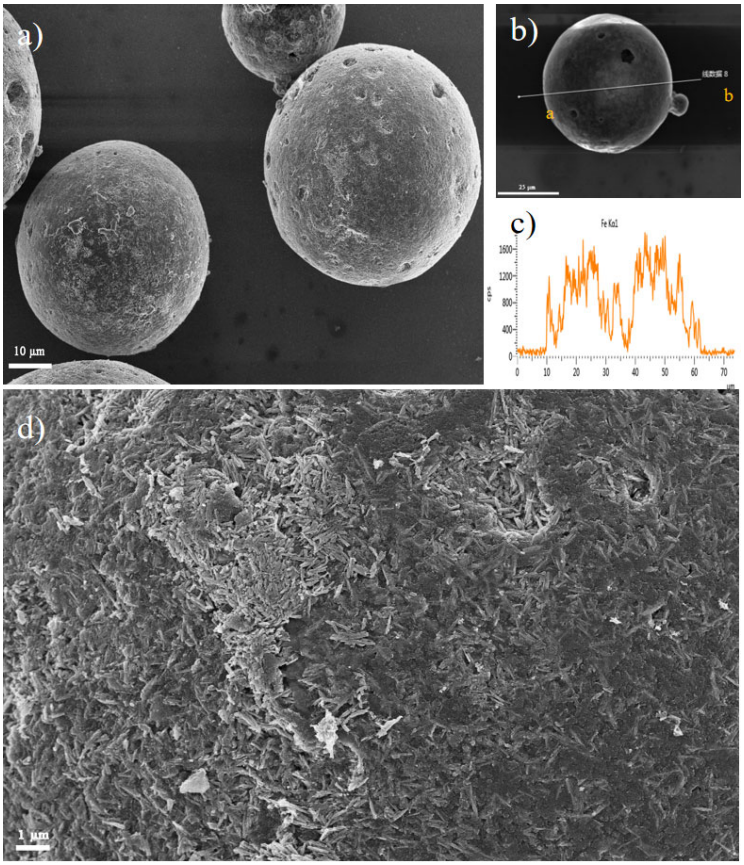


**Figure 3. a**) SEM image of MAER, **b**) EDS element line-scanning of MAER, **c**) the Fe element signal of image b) along a line to b, and **d**) SEM image of MAER in high magnification.

*3.2. Adsorption of X-3B*

The adsorption behavior of X-3B on these three synthesized materials ($Fe_3O_4$, AER, and MAER) was evaluated in the absence of $H_2O_2$ and a UV lamp at pH = 7.0 (Figure S6). The adsorption capacity showed a rapid increase in the first 6 h and then increased slowly before reaching equilibrium. The adsorption capacities of $Fe_3O_4$, AER, and MAER were 96.0 mg/g, 28.8 mg/g, and 185.6 mg/g, respectively, after adsorption for 24 h. About 92% of X-3B (50 mg/L) was removed by the MAER. The adsorption performance of the resin after magnetization showed an obvious improvement. The charge property of the adsorbents is an important factor for adsorption. Therefore, the zeta potential of the synthesized materials was measured (Figure S7). Compared with the electronegative property of $Fe_3O_4$, the MAER after polymerization became electropositive at a wide pH range from 3.0 to 11.0. The pseudo-first-order model (Equation (1)) and pseudo-second-order model (Equation (2)) were used to investigate the adsorption kinetics:

$$Q_t = Q_e \times (1\text{-}e^{-k_1 t}) \quad (1)$$

$$\frac{t}{Q_t} = \frac{1}{Q_e} t + \frac{1}{k_2 Q_e^{\,2}} \quad (2)$$

where $Q_e$ (mg/g) is the adsorption capacity at the equilibrium state, t (h) is the predetermined time, $k_1$ ($h^{-1}$) is the pseudo-first-order adsorption rate constant, and $k_2$ (g/(mg h)) is the pseudo-second-order adsorption rate constant.

The obtained relevant adsorption parameters are shown in Table 1. All these materials tended to fit better using the pseudo-second-order model than that of the

pseudo-first-order model. The adsorption process may have both physical adsorption and chemical adsorption [28,29]. It could be concluded that the MAER had better adsorption capacity for the removal of X-3B from water.

**Table 1.** Kinetic parameters of adsorption process.

| Samples | Pseudo-first-order | | | Pseudo-second-order | | |
|---|---|---|---|---|---|---|
| | $k_1$ ($h^{-1}$) | $Q_e$ (mg/g) | $R^2$ | $k_2$ (g/mg/h) | $Q_e$ (mg/g) | $R^2$ |
| $Fe_3O_4$ | 0.13 | 96.7 | 0.936 | $1.10\times10^{-3}$ | 121.5 | 0.953 |
| AER | 1.06 | 25.0 | 0.772 | $4.92\times10^{-2}$ | 27.3 | 0.788 |
| MAER | 0.53 | 182.6 | 0.983 | $3.11\times10^{-3}$ | 208.7 | 0.989 |

$k_1$: the pseudo-first-order adsorption rate constant; $k_2$: the pseudo-second-order adsorption rate constant; $Q_e$: the adsorption capacity at the equilibrium state.

### *3.3. Removal of X-3B in a UV–Fenton System*

The removal of X-3B in different reaction systems was investigated (Figure 4a). When bare UV was used in the absence of the Fenton reagent, X-3B could not be removed over the 30 min irradiation time-scales. Through calculation, only 0.54% of X-3B was removed in 30 min MAER adsorption alone (Figure S6). In the presence of $H_2O_2$ alone, only 22% of the X-3B was removed. For the $Fe_3O_4/H_2O_2$ UV–Fenton system, 61% of the X-3B could be removed within 30 min. When MAER instead of $Fe_3O_4$ was used as the catalyst, more than 99% of X-3B was removed within 20 min. This observation suggests that the MAER had great catalytic reactivity for the UV–Fenton reactions.

The effects of $H_2O_2$ dose, X-3B initial concentration, and initial pH value on the X-3B removal efficiency were investigated in a MAER UV–Fenton system. In general, high levels of $H_2O_2$ are beneficial for the generation of reactive radicals via chain reaction. However, an obvious inhibitory effect was observed when the concentration of $H_2O_2$ was increased from 250 mM to 1000 mM (Figure 4b). This effect was probably due to the scavenging effect of $H_2O_2$ toward reactive radicals [30]. The initial concentration of X-3B also had an effect on the removal efficiency (Figure 4c). The rates of removal decreased when increasing the initial concentration of X-3B from 20 mg/L to 100 mg/L. This result is consistent with the existing adsorption-catalysis equilibrium at the solid–liquid interface [31]. The pH value is an important parameter in wastewater treatment, and thus, the reactivity of MAER under different pH values was explored (Figure 4d). Higher removal efficiencies were observed at pH values of 3.0 and 5.0 than at 7.0 and 9.0, suggesting that an acidic environment is beneficial for the UV–Fenton system [32,33].

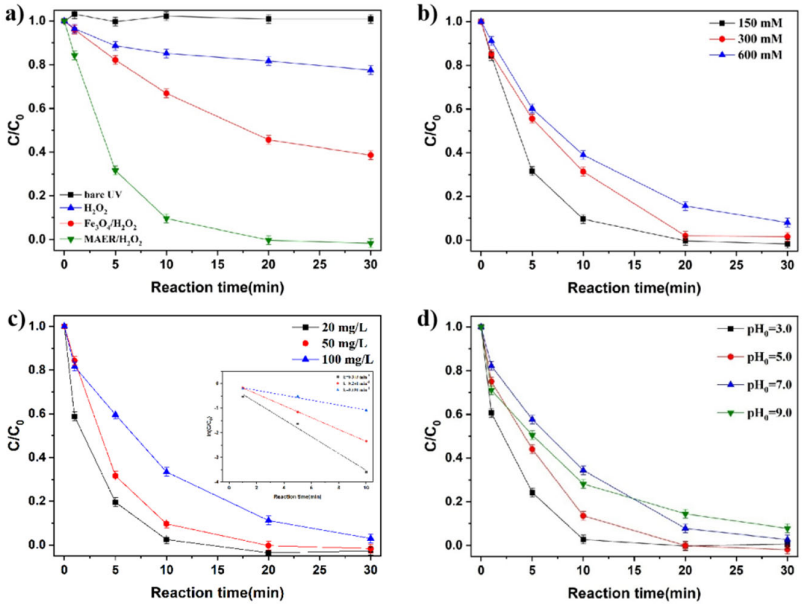


**Figure 4. a**) Removal of X-3B by different reaction systems, effects of **b**) $H_2O_2$ dosage, **c**) initial concentration of X-3B, and **d**) initial pH value on removal efficiency of X-3B in a MAER UV–Fenton system. Reaction conditions (unless otherwise specified): $C_{0,\,X\text{-}3B}$ = 50 mg/L, [Material] = 0.25 g/L, [$H_2O_2$] = 150 mM, T = 25 °C, and pH with no adjustment.

The generation of reactive radicals in the UV–Fenton system was investigated by ESR experiments. As shown in Figure 5a, four peaks with an intensity ratio of 1:2:2:1 were recorded in the MAER UV–Fenton system after a reaction for 10 min, which suggests the generation of •OH [34]. Typical peaks of the spin adduct DMPO/•$O_2^-$ at the intensity ratio of 1:1:1:1 was also detected (Figure 5b). Thus, •$O_2^-$ was also generated in the catalytic system in addition to •OH. Meanwhile, similar signals were observed with $Fe_3O_4$, but their intensity was much weaker, which suggests that MAER was more efficient than $Fe_3O_4$ for the generation of reactive radicals [35,36].

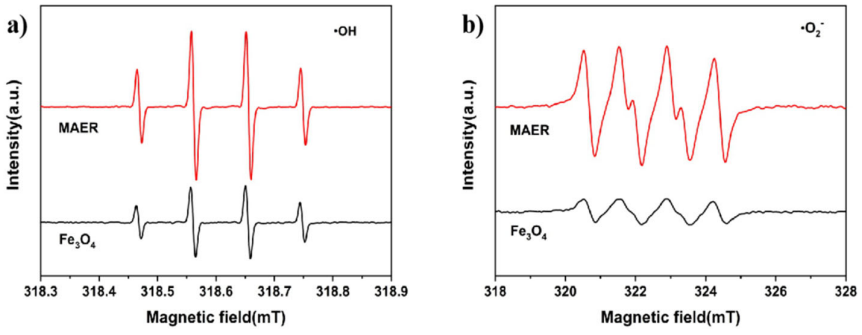


**Figure 5.** Electron spin resonance (ESR) spectra of different catalytic systems using 5,5-dimethyl-1-pyrroline N-oxide (DMPO) spin-trapping: **a**) •OH and **b**) •$O_2$-. Reaction conditions: $C_{0,\,X\text{-}3B}$ = 50 mg/L, [Material] = 0.25 g/L, [$H_2O_2$] = 150 mM, [DMPO] = 100 mM, T = 25 °C, and pH with no adjustment.

UV-Vis spectroscopy was used to analysis the removal of X-3B (Figure 6a). The absorption peak of X-3B near 539 nm gradually disappeared with the increase in reaction

time, proving that the chromogenic group of the N=N bond in X-3B was decomposed [37]. Meanwhile, the solution of X-3B was obviously faded after the catalytic reaction.

To explore the contribution of radicals to the removal of X-3B, classical scavenging experiments were also conducted. Tert-butanol and chloroform are usually used as the quenching agents of •OH (k= $7.6\times10^8$ $M^{-1}$ $s^{-1}$) and $•O_2^-$ (k = $3.0\times10^{10}$ $M^{-1}$ $s^{-1}$), respectively [14,38–40]. As shown in Figure 6b, the removal of X-3B was inhibited by the presence of either *tert*-butanol or chloroform, revealing the contribution of generated •OH and $•O_2^-$ to the oxidative removal of X-3B in the MAER UV–Fenton system. After a reaction of 30 min, the removal efficiencies of X-3B were decreased to 55% and 46% by adding 261 mM and 522 mM of *tert*-butanol, respectively. Chloroform had a relatively weaker quenching effect; X-3B still had 79% and 71% removal efficiencies in the presence of 261 mM and 522 mM chloroform, respectively. Thus, the •OH radical should be the main reactive species during the MAER UV–Fenton system and the $•O_2^-$ radicals play a vital role in accelerating the generation of •OH radicals.

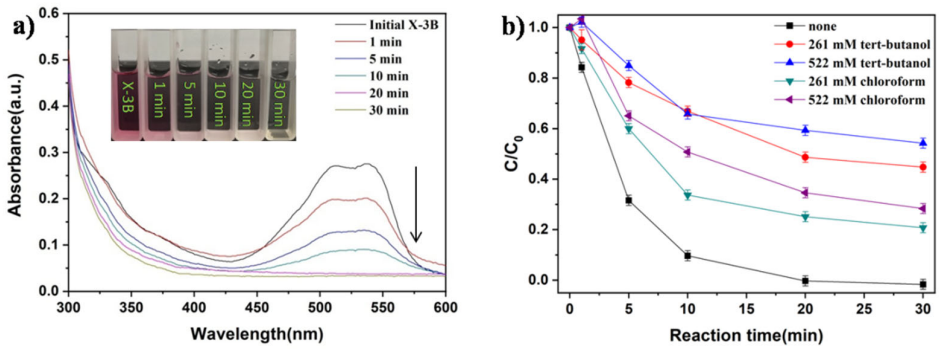


**Figure 6. a**) UV-Vis spectroscopy and color change (inset) in X-3B for different reaction periods; **b**) quenching effects of tert-butanol and chloroform on the removal of X-3B in the MAER UV–Fenton system. Reaction conditions: $C_{0,\text{X-3B}}$ = 50 mg/L, [Material] = 0.25 g/L, [$H_2O_2$] = 150 mM, T = 25 °C, and pH with no adjustment.

MAER could work as the heterogeneous UV–Fenton catalyst with higher catalytic activity for the removal of X-3B. This might be explained as follows: First, uniformly dispersed core-shell magnetic microsphere resin could suppress the aggregation of $Fe_3O_4$ nanoparticles and enhance the exposure of Fe sites for arousing catalytic reaction with $H_2O_2$. Second, the good adsorption capacity of MAER with mesoporous structure played an important role in improving contact between X-3B and reactive radicals in the Fenton reaction. When the system was excited by UV irradiation, it generated photo electrons, was quickly captured, stabilized on the MAER surface, and then was transferred to the $Fe_3O_4$ magnetic core to accelerate the Fe(Ⅲ) transform to Fe(Ⅱ), which is beneficial for the generation of more reactive radicals. The removal of MAER for X-3B could be ascribed to the synergistic effect of its catalytic activity and adsorption capacity in the UV–Fenton system.

### *3.4. Practical Application for Removal of Textile Dyeing Wastewater*

The effects of common water components including $Cl^-$, $NO_3^-$, $SO_4^{2-}$, and HA on the removal of X-3B were investigated to evaluate the potential practical application of the MAER UV–Fenton system. The removal of X-3B was followed by pseudo-first-order kinetics, and the results are shown in the inset of Figure S8. The kinetics mode was used: $\ln(C_0/C) = kt$, where t (min) is the reaction time and k ($min^{-1}$) is the apparent rate constant for the MAER catalyst [41]. The results showed that $Cl^-$ inhibited the removal of X-3B in a low concentration. The $Cl^-$ may form a dichloride radical anion ($•Cl_2^-$) in the MAER UV–Fenton system, which was less reactive with dyes. The excess $Cl^-$ also could scavenge reactive radicals and then reduce the X-3B removal efficiency [42]. The $NO_3^-$ could react

with •OH to produce a nitrate radical (•$NO_3$). However, the reactivity of •$NO_3$ was also less than •OH, resulting in decreased removal efficiency of X-3B [43]. The addition of $SO_4^{2-}$ could be beneficial to improve the removal of X-3B. Generally, $SO_4^{2-}$ reacted with •OH could form •$SO_4^-$ radicals. The redox potential of •$SO_4^-$ was higher than •OH, further improving the removal efficiency of X-3B [44]. Natural organic matter was represented by HA in this work. It showed that the presence of HA reduced the X-3B removal efficiency with an increasing concentration of HA. This is because the electron-rich moieties of HA molecules are easily attacked by •OH and •$O_2^-$ radicals, leading to competition reaction between HA and X-3B. The SEM of the MAER before and after the UV–Fenton reaction were tested as shown in Figure S9. Overall, the MAER-mediated UV–Fenton system maintains stable and efficient removal efficiency for X-3B dye under the influence of different substrates in water environment.

The TOC removal of X-3B and the actual textile dyeing wastewater in a MAER-mediated UV–Fenton system was investigated. As seen from Figure 7, 42.3% and 56.9% TOC of the X-3B solution was removed after 30 min and 60 min of MAER UV–Fenton reactions, respectively. This result is consistent with Figure 4a above, indicating that X-3B can be mineralized by the MAER-mediated UV–Fenton process. The actual textile dyeing wastewater was also used for testing, and the removal rate of TOC reached 17.4%, decreasing from 78.0 mg/L to 64.3 mg/L. The TOC results confirmed that the established MAER-mediated UV–Fenton system had better processing capacity for X-3B than that for the actual textile dyeing wastewater. Meanwhile, the color of X-3B and actual textile dyeing wastewater also obviously faded out after the UV–Fenton reaction, as shown in Figure S10.

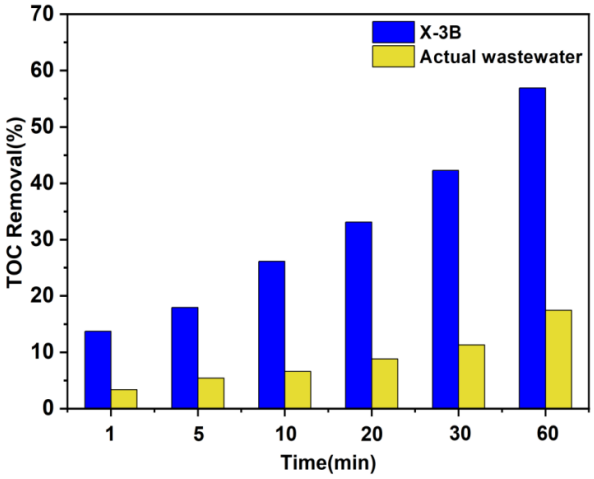


**Figure 7.** The total organic carbon (TOC) removal of X-3B and actual textile dyeing wastewater in a MAER UV–Fenton system. Reaction conditions: $C_{0,\text{X-3B}}$ = 50 mg/L, $TOC_{0,\text{actual}}$ = 78.0 mg/L, [$H_2O_2$] = 150 mM, [Material] = 0.25 g/L, T = 25 °C, and pH with no adjustment.

## 4. Conclusions

An efficient core-shell MAER catalyst was prepared through in situ polymerization and used to remove X-3B in the heterogeneous UV–Fenton system. The MAER exhibited satisfactory removal efficiency for X-3B and could be easily separated by a magnet after catalytic reactions. The mechanism research showed that •OH radical was the main reactive species for the removal of X-3B. Moreover, common water components including $Cl^-$, $NO_3^-$, $SO_4^{2-}$, and HA had limited influence on the removal of X-3B. The MAER-mediated UV–Fenton system had high TOC removal capability for X-3B and actual textile dyeing wastewater. These results suggest that the catalytic oxidation system established in the current study is promising for practical wastewater remediation applications.

**Supplementary Materials:** The following are available online at www.mdpi.com/2073-4441/13/7/968/s1, Figure S1: The actual textile dyeing wastewater collected from a textile dyeing industrial factory in Guangxi Province. Figure S2: The UV light signal in the range 200–800 nm. Figure S3: XPS spectra of Fe 2p for the MAER catalyst. Figure S4: The SEM image of $Fe_3O_4$. Figure S5: a) $N_2$ adsorption/desorption isotherm of MAER; b) The BJH (Barrett, Joyner and Halenda) pore size distribution of MAER. Figure S6: Adsorption behavior of X-3B on three synthesized materials. Figure S7: Zeta potentials of $Fe_3O_4$ and MAER in different solution pH values. Figure S8: Matrix effects of a) $Cl^-$, b) $NO_3^-$, c) $SO_4^{2-}$, and d) HA on X-3B removal in a MAER UV–Fenton system. Reaction conditions: $C_{0,\,X\text{-}3B}$ = 50mg/L, [Material] = 0.25 g/L, [$H_2O_2$] = 150 mM, T = 25°C, and pH with no adjustment. Figure S9: SEM images of MAER a) before and b) after a UV–Fenton reaction. Figure S10: a) X-3B sample and b) actual wastewater sample collected at different reaction times, X-3B sample c) before and d) after a UV–Fenton reaction, and an actual wastewater sample e) before and f) after a UV–Fenton reaction. Table S1: Properties of the selected dye. Table S2: Properties of an actual textile dyeing wastewater sample. Table S3: Surface structural properties of MAER.

**Author Contributions:** J.Z.: investigation, methodology, data curation, and writing—original draft preparation, B.Y.: methodology, writing—review and editing, and supervision, Y.F.: methodology and writing—review and editing, Y.C.: resources, L.-G.W.: resources, W.-D. Y.: analysis, G.-G.Y.: resources and supervision. All authors have read and agreed to the published version of the manuscript.

**Funding:** We would like to acknowledge the financial support from the Scientific Research and Technology Development Program of Guangxi (2018AB36018) and from the National Natural Science Foundation of China (NSFC U1701242, 42030703, and 41877358). Dr. Bin Yang acknowledges the Pearl River Talent Plan of Guangdong Province (2017GC010244) and Guangdong Provincial Key Laboratory of Chemical Pollution and Environmental Safety (2019B030301008).

**Institutional Review Board Statement:** Not applicable.

**Informed Consent Statement:** Not applicable.

**Data Availability Statement:** Not applicable.

**Conflicts of Interest:** The authors declare no competing financial interest.

## References

1. Tang, S.; Li, N.; Yuan, D.; Tang, J.; Li, X.; Zhang, C.; Rao, Y. Comparative study of persulfate oxidants promoted photocatalytic fuel cell performance: Simultaneous dye removal and electricity generation. *Chemosphere* **2019**, *234*, 658–667.
2. Devi, L.G.; Kumar, S.G.; Reddy, K.M.; Munikrishnappa, C. Photo degradation of Methyl Orange an azo dye by Advanced Fenton Process using zero valent metallic iron: Influence of various reaction parameters and its degradation mechanism. *J. Hazard. Mater.* **2009**, *164*, 459–467.
3. Zhou, G.; Guo, J.; Zhou, G.; Wan, X.; Shi, H. Photodegradation of Orange II using waste paper sludge-derived heterogeneous catalyst in the presence of oxalate under ultraviolet light emitting diode irradiation. *J. Environ. Sci.* **2016**, *47*, 63–70.
4. Xu, J.; Wang, X.; Pan, F.; Qin, Y., Xia, J., Li, J., & Wu, F. Synthesis of the mesoporous carbon-nano-zero-valent iron composite and activation of sulfite for removal of organic pollutants. *Chem. Eng. J.* **2018**, *353*, 542–549.
5. Yang, B.; Ying, G.G. Oxidation of benzophenone-3 during water treatment with ferrate (VI). *Water Res.* **2013**, *47*, 2458–2466.
6. Wang, H.; Zhang, L.; Hu, C.; Wang, X., Lyu, L.; Sheng, G. Enhanced degradation of organic pollutants over Cu-doped $LaAlO_3$ perovskite through heterogeneous Fenton-like reactions. *Chem. Eng. J.* **2018**, *332*, 572–581.
7. Dodd, M.C.; Buffle, M.O.; Von Gunten, U. Oxidation of antibacterial molecules by aqueous ozone: Moiety-specific reaction kinetics and application to ozone-based wastewater treatment. *Environ. Sci. Technol.* **2006**, *40*, 1969–1977.
8. Samy, M.; Ibrahim, M.G.; Alalm, M.G.; Fujii, M., Ookawara, S.; Ohno, T. Photocatalytic degradation of trimethoprim using S-$TiO_2$ and Ru/$WO_3$/$ZrO_2$ immobilized on reusable fixed plates. *J. Water Process Eng.* **2020**, *33*, 101023.
9. Michael, I.; Hapeshi, E.; Osorio, V.; Perez, S.; Petrovic, M.; Zapata, A.; Malato, S.; Fatta-Kassinos, D. Solar photocatalytic treatment of trimethoprim in four environmental matrices at a pilot scale: Transformation products and ecotoxicity evaluation. *Sci. Total Environ.* **2012**, *430*, 167–173.
10. Hou, Y.; Peng, Z.; Wang, L.; Yu, Z.; Huang, L.; Sun, L.; Huang, J. Efficient degradation of tetrabromobisphenol A via electrochemical sequential reduction-oxidation: Degradation efficiency, intermediates, and pathway. *J. Hazard. Mater.* **2018**, *343*, 376–385.
11. Yuan, D.; Zhang, C.; Tang, S.; Li, X.; Tang, J.; Rao, Y.; Wang Z.; Zhang, Q. Enhancing $CaO_2$ fenton-like process by Fe(II)-oxalic acid complexation for organic wastewater treatment. *Water Res.* **2019**, *163*, 114861.

12. Lin, S.S; Gurol, M.D. Catalytic decomposition of hydrogen peroxide on iron oxide: Kinetics, mechanism, and implications. Environ. *Sci. Technol.* **1998**, *32*, 1417–1423.
13. Engelmann, M.D.; Bobier, R.T.; Hiatt, T.; Cheng, I. F. Variability of the Fenton reaction characteristics of the EDTA, DTPA, and citrate complexes of iron. *Biometals* **2003**, *16*, 519–527.
14. Pan, Y.; Su, H.; Zhu, Y.; Molamahmood, H. V.; Long, M. $CaO_2$ based Fenton-like reaction at neutral pH: Accelerated reduction of ferric species and production of superoxide radicals. *Water Res.* **2018**, *145*, 731–740.
15. Samy, M.; Ibrahim, M.G.; Alalm, M.G.; Fujii, M. MIL-53(Al)/ZnO coated plates with high photocatalytic activity for extended degradation of trimethoprim via novel photocatalytic reactor. *Sep. Purif. Technol.* **2020**, *249*, 117173.
16. Feng, Y.; Zhang, L.; Yang, Z.; Fan, Y.; Shih, K.; Li, H.; Liu, Y.; Wu, D. Nonradical degradation of microorganic pollutants by magnetic N-doped graphitic carbon: A complement to the unactivated peroxymonosulfate. *Chem. Eng. J.* **2020**, *392*, 123724.
17. Xu, H.Y.; Li, B.; Shi, T.N.; Wang, Y.; Komarneni, S. Nanoparticles of magnetite anchored onto few-layer graphene: A highly efficient Fenton-like nanocomposite catalyst. *J. Colloid Interf. Sci.* **2018**, *532*, 161–170.
18. Hu, X.; Liu, B.; Deng, Y.; Chen, H.; Luo, S.; Sun, C.; Yang, P.; Yang, S. Adsorption and heterogeneous Fenton degradation of 17$\alpha$-methyltestosterone on nano $Fe_3O_4$/MWCNTs in aqueous solution. *Appl. Catal. B Environ.* **2011**, *107*, 274–283.
19. Gong, Q.; Liu, Y.; Dang, Z. Core-shell structured $Fe_3O_4$@GO@MIL-100(Fe) magnetic nanoparticles as heterogeneous photo-Fenton catalyst for 2, 4-dichlorophenol degradation under visible light. *J. Hazard. Mater.* **2019**, *371*, 677–686.
20. Shuang, C.; Li, P.; Li, A.; Zhou, Q.; Zhang, M.; Zhou, Y. Quaternized magnetic microspheres for the efficient removal of reactive dyes. *Water Res.* **2012**, *46*, 4417–4426.
21. Lyu, Y.; Kim, J.H.; Gu, X. Developing methodology for service life prediction of PV materials: Quantitative effects of light intensity and wavelength on discoloration of a glass/EVA/PPE laminate. *Sol. Energy* **2018**, *174*, 515–526.
22. Davarpanah, M.; Ahmadpour, A.; Bastami, T.R. Preparation and characterization of anion exchange resin decorated with magnetite nanoparticles for removal of p-toluic acid from aqueous solution. *J. Magn. Magn. Mater.* **2015**, *375*, 177–183.
23. Tan, L.; Xu, J.; Xue, X.; Lou, Z.; Zhu, J.; Baig, S. A.; Xu, X. Multifunctional nanocomposite $Fe_3O_4$@$SiO_2$–mPD/SP for selective removal of Pb(Ⅱ) and Cr(Ⅵ) from aqueous solutions. *RSC Adv.* **2014**, *4*, 45920–45929.
24. Peng, S.; Zhang, W.; He, J.; Yang, X.; Wang, D.; Zeng, G. Enhancement of Fenton oxidation for removing organic matter from hypersaline solution by accelerating ferric system with hydroxylamine hydrochloride and benzoquinone. *J. Environ. Sci.* **2016**, *41*, 16–23.
25. Al-Anazi, A.; Abdelraheem, W.H.; Scheckel, K.; Nadagouda, M. N.; O'Shea, K.; Dionysiou, D. D. Novel franklinite-like synthetic zinc-ferrite redox nanomaterial: Synthesis, and evaluation for degradation of diclofenac in water. *Appl. Catal. B Environ.* **2020**, *275*, 119098.
26. Xu, L.; Wang, J. Fenton-like degradation of 2, 4-dichlorophenol using $Fe_3O_4$ magnetic nanoparticles. *Appl. Catal. B Environ.* **2012**, *123*, 117–126.
27. Du, Y.K.; Yang, P.; Mou, Z.G.; Hua, N. P.; Jiang, L. Thermal decomposition behaviors of PVP coated on platinum nanoparticles. *J. Appl. Polym. Sci.* **2006**, *99*, 23–26.
28. Babaeivelni, K.; Khodadoust, A.P.; Bogdan, D. Adsorption and removal of arsenic (V) using crystalline manganese (II, III) oxide: Kinetics, equilibrium, effect of pH and ionic strength. *J. Environ. Sci. Health A* **2014**, *49*, 1462–1473.
29. Zhong, J.; Feng, Y.; Li, J.L.; Yang, B.; Ying, G. G. Removal of Sulfadiazine Using 3D Interconnected Petal-Like Magnetic Reduced Graphene Oxide (MrGO) Nanocomposites. *Water* **2020**, *12*, 1933.
30. Xu, J.; Ding, W.; Wu, F.; Mailhot, G.; Zhou, D.; Hanna, K. Rapid catalytic oxidation of arsenite to arsenate in an iron (III)/sulfite system under visible light. *Appl. Catal. B Environ.* **2016**, *186*, 56–61.
31. Liu, Z.; Yang, S.; Yuan, Y.; Xu, J.; Zhu, Y.; Li, J.; Wu, F. A novel heterogeneous system for sulfate radical generation through sulfite activation on a $CoFe_2O_4$ nanocatalyst surface. *J. Hazard. Mater.* **2017**, *324*, 583–592.
32. Zheng, C.M.; Yang, C.W.; Cheng, X.Z.; Xu, S.C.; Fan, Z.P.; Wang, G.H.; Wang, S.B.; Guan, X.F.; Sun, X.H. Specifically enhancement of heterogeneous Fenton-like degradation activities for ofloxacin with synergetic effects of bimetallic Fe-Cu on ordered mesoporous silicon. *Sep. Purif. Technol.* **2017**, *189*, 357–365.
33. Yuan, Y.; Yang, S.; Zhou, D.; Wu, F. A simple Cr(VI)–S(IV)–$O_2$ system for rapid and simultaneous reduction of Cr (VI) and oxidative degradation of organic pollutants. *J. Hazard. Mater.* **2016**, *307*, 294–301.
34. Wei, Z.; Villamena, F.A.; Weavers, L.K. Kinetics and mechanism of ultrasonic activation of persulfate: An in situ EPR spin trapping study. *Environ. Sci. Technol.* **2017**, *51*, 3410–3417.
35. Liu, Y.; Sun, N.; Chen, S.; Yan, R.; Li, P.; Qu, Y.; Jing, L. Synthesis of nano $SnO_2$-coupled mesoporous molecular sieve titanium phosphate as a recyclable photocatalyst for efficient decomposition of 2, 4-dichlorophenol. *Nano Res.* **2018**, *11*, 1612–1624.
36. Brillas, E.; Sirés, I.; Oturan, M.A. Electro-Fenton process and related electrochemical technologies based on Fenton's reaction chemistry. *Chem. Rev.* **2009**, *109*, 6570–6631.
37. Diao, Z.H.; Liu, J.J.; Hu, Y.X.; Kong, L.J.; Jiang, D.; Xu, X.R. Comparative study of Rhodamine B degradation by the systems pyrite/$H_2O_2$ and pyrite/persulfate: Reactivity, stability, products and mechanism. *Sep. Purif. Technol.* **2017**, *184*, 374–383.
38. Anipsitakis, G.P.; Dionysiou, D.D. Radical generation by the interaction of transition metals with common oxidants. *Environ. Sci. Technol.* **2004**, *38*, 3705–3712.
39. Buxton, G.V.; Greenstock, C.L.; Helman, W.P.; Ross, A.B. Critical review of rate constants for reactions of hydrated electrons, hydrogen atoms and hydroxyl radicals (·OH/·$O^-$ in aqueous solution. *J. Phys. Chem. Ref. Data* **1988**, *17*, 513–886.

40. Wilkinson, F.; Helman, W.P.; Ross, A.B. Rate constants for the decay and reactions of the lowest electronically excited singlet state of molecular oxygen in solution: An expanded and revised compilation. *J. Phys. Chem. Ref. Data* **1995**, *24*, 663–677.
41. Xu, H.Y.; Shi, T.N.; Wu, L.C.; Qi, S. Y. Discoloration of methyl orange in the presence of schorl and $H_2O_2$: Kinetics and mechanism. *Water Air Soil Poll.* **2013**, *224*, 1–11.
42. Zhang, X.; Gu, X.; Lu, S.; Miao, Z.; Xu, M.; Fu, X.; Qiu, Z.; Sui, Q. Degradation of trichloroethylene in aqueous solution by calcium peroxide activated with ferrous ion. *J. Hazard. Mater.* **2015**, *284*, 253–260.
43. Jin, Y.; Sun, S.P.; Yang, X.; Chen, X. D. Degradation of ibuprofen in water by $Fe^{II}$-NTA complex-activated persulfate with hydroxylamine at neutral pH. *Chem. Eng. J.* **2018**, *337*, 152–160.
44. Zhang, X.; Gu, X.; Lu, S.; Miao, Z.; Xu, M.; Fu, X.; Qiu; Z.; Sui, Q. Application of calcium peroxide activated with Fe(II)-EDDS complex in trichloroethylene degradation. *Chemosphere* **2016**, *160*, 1–6.